Supplementary Information

Nonmonotonic Thickness-dependence of In-plane Thermal Conductivity of Few-Layered MoS_2: 2.4 to 37.8 nm

Pengyu Yuan[1,§], Ridong Wang[1,§], Tianyu Wang[1], Xinwei Wang[1,*], Yangsu Xie[2,*]

[1]Department of Mechanical Engineering, Iowa State University, Ames, IA 50011, USA

[2]College of Chemistry and Environmental Engineering, Shenzhen University, Shenzhen, Guangdong, 518055, P. R. China

* Correspondence: xwang3@iastate.edu (X.W.); ysxie@szu.edu.cn (Y.X.)

§ These authors contributed equally to this work.

S1. Additional physical model details for two picosecond-pulsed laser heating states

For CW and ps lasers used in this work, choosing the same wavelength for them ensures that the samples have the same laser absorption level for all five heating states. Under steady-state, the Raman signal gives the temperature profile of the interested material under equilibrium. In the transient state by picosecond laser Raman, due to the ultra-short laser pulse (13 ps) and long relaxation time (20 ns), we consider the non-equilibrium process. However, like graphene, the relaxation between hot carriers and optical phonons is only ~100 fs, and the relaxation of the resulting hot optical phonons with acoustic phonons is around 2~3 ps.[1-3] All these timescales are smaller than our laser pulse which is 13 ps, so the temperature profile obtained from picosecond laser Raman gives the acoustic phonon in equilibrium. In the two ps laser heating states, within the short heating time (t_0=13 ps), the thermal diffusion length (L_t) for MoS_2 and glass substrate is estimated to be around 38 nm and 6.6 nm, respectively. ($L_t = 2\sqrt{\alpha_k t_0}$, α_k=2.75×10^{-5} m^2/s for MoS_2 and 8.26×10^{-7} m^2/s for glass,[4] is the in-plane thermal diffusivity). They are all much smaller than the ps laser spot size (diameter is 0.923 μm under 50× and 0.521 μm under 100× objective). On the other hand, we also estimate the thermal relaxation time (TRT, the time taken for the sample to dissipate about 63% of the incident thermal energy) of the MoS_2 nanosheets for our interface structure. TRT is estimated to be around 4.5–71.4 ns (=$z\cdot\rho c_p\cdot R$. z ranges from 2.4 nm to 37.8 nm and is the thickness of MoS_2 nanosheets; ρc_p=1.89 MJ/m^3·K, is the volumetric heat capacity, R takes 10^{-6} K·m^2/W, is a typical interface thermal resistance.). Some of the samples even have a TRT that is longer than the laser cooling time (20.8 ns). As a result, the energy absorbed at the focal volume from each pulse does not have sufficient time to diffuse out before the next pulse comes in, thus forming a point source of heating. The temperature rise measured by Raman

spectroscopy in ps laser heating comes from two parts: single pulse heating and steady-state accumulation heating. Due to the different heating size from 100× and 50× objectives, the temperature rise from a single pulse is different. During first several pulses heating, the temperature rises from steady-state accumulation at 100× and 50× objective are also different due to the heating size effect. Nevertheless, as time goes on under same power level (1 mW), this difference will get smaller and disappear. Within one heating period (20.8 ns), the thermal diffusion length (L_t) of MoS_2 is 1.513 μm (lateral direction). ($L_t = 2\sqrt{\alpha_k t_c}$, t_c=20.8 ns). Also, the hot carrier diffusion could also extend the heating size (in the order of 300 nm).[5] Consequently, considering the original laser heating size, thermal diffusion and hot carrier diffusion, the heating size (radius) at the end of each heating period is expanded to around 2.073 μm and 2.273 μm for 100× and 50× objectives, respectively. During the Raman experiment, this small difference will be negligible when the thermal equilibrium is reached. Additionally, the heating power from a single pulse is around 1600 time larger than its average level (P_{peak}×13 ps = P_{avg}×20.8 ns). And the temperature distribution is much more uniform from heat accumulation than from single-pulse heating. The measured RSC reflects the space average weighted temperature as expressed in Eq. S1 and S2. The contribution from heat accumulation is much smaller. As a result, the measured temperature rise (T_s) from the steady-state accumulation at 100× and 50× can be treated the same. For the thin samples whose TRT is much smaller than the laser cooling time, there is no steady-state heat accumulation effect and the measured temperature rise difference between at 100× and 50× is only from the single pulse heating.

In our experiment, the overall Raman wavenumber change induced by laser heating is around 1.5 cm^{-1}. The Raman temperature coefficient is estimated from our previous work[6] as 0.02 cm^{-1}/K.

The absolute temperature rise induced by the highest laser power is around 75 K. Additionally, the free carrier density at equilibrium could be given as $n_0 = N_s \exp(-E_g / 2k_B T)$, where N_s is the number per unit volume of effectively available states. It is in the of order 10^{19} cm^{-3} at room temperature and increases with temperature. k_B is the Boltzmann's constant. At room temperature, $k_B T$ = 0.026 eV. So $k_B T \ll E_g (1.38\ \text{eV})$ gives a very small n_0 (room temperature) to neglect the thermal activation term.

In this technique for different heating states in supported 2D material, we ignore the heat loss (radiation or natural convection) to the environment during the Raman measurement.[7] Also, the measured RSC with CW laser represents the temperature rise which is a Raman/laser intensity weighted average over the laser spot size as

$$\overline{T}_{\text{CW}} = \int_0^{V_0} I_a(\boldsymbol{r}) T(\boldsymbol{r}) dv \,/\, \int_0^{V_0} I_a(\boldsymbol{r}) dv \,. \tag{S1}$$

For the ps laser heating states, the RSC will include both time and space averaged over the pulse width and heating domain as

$$\overline{T}_{\text{ps}} = \int_0^{t_0} \int_0^{V_0} I_a(\boldsymbol{r},t) T(\boldsymbol{r},t) dv \,/\, \int_0^{t_0} \int_0^{V_0} I_a(\boldsymbol{r},t) dv \,. \tag{S2}$$

S2. Schematic of Five State ET-Raman experiment setup

As shown in Figure S1, the Raman experiments are performed by using a confocal Raman system that consists of a Raman spectrometer (Voyage™, B&W Tek, Inc.) and a microscope (Olympus BX53). The 532 nm CW laser or ps laser is introduced to the Raman system and the laser power is adjusted by a motorized neutral-density (ND) filter system (CONEX-NSR1 and NSND-5,

Newport Corporation). To search for and identify the MoS_2 sample under the microscope, we use a 3D piezo-actuated nano-stage (MAX313D, Thorlabs, Inc.) During the experiment, the laser beam is focused on a specific area of the samples (as shown in Fig. 1).

During the experiments, we use the LabVIEW-based program to fully control the Raman spectrometer, the motorized ND filter, and 3D nano-stage. The Raman spectrometer could automatically acquire and store the spectrum for each energy level by setting the ND filter position to get RSC for different heating states. This design could considerably shorten the experiment time to reduce the environmental noise and improve the precision of the RSC determination.

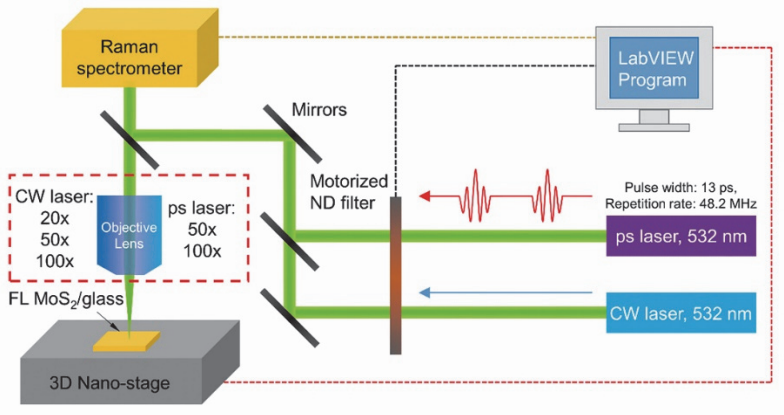

Figure. S1 Schematic of ET-Raman experiment setup. A typical MoS_2/glass sample is mounted on a 3D nano-stage and illuminated by CW or ps 532 nm laser. The same laser source is used to excite the Raman signals which are collected by a confocal Raman spectrometer. The laser power is adjusted by a motorized ND filter. Three objective lenses are used in CW laser heating, and two are used in ps laser heating.

S3. Five-State ET-Raman experiment results summary

Few-layered MoS_2 nanosheets have thickness dependent bandgap due to quantum confinement.[8, 9] In this work, based on Yim *et al*.' work,[8] we fit the E_g values against the thickness by an exponential function $[E_g(\text{eV}) = 0.5836 \times \exp(-\text{thickness} / 3.525) + 1.29]$ and extract the E_g values for our samples as shown in Table S1.

Table S1. Summary of Raman experiment results of eight MoS_2 samples. The steady-state Raman shift power coefficient (RSC) values under 20×, 50× and 100× objective with CW laser (χ_{CW1} , χ_{CW2} and χ_{CW3}) for E^1_{2g} mode of MoS_2. The zero-transport state RSC values under 50× and 100× objective with ps laser (χ_{ps1} and χ_{ps2}). Also the normalized RSC (Θ_{exp_1}, Θ_{exp_2} and Θ_{exp_3}).

Sample thickness	**Band gap (eV)**	χ_{CW1} **(cm^{-1}/mW)**	χ_{CW2} **(cm^{-1}/mW)**	χ_{CW3} **(cm^{-1}/mW)**	χ_{ps1} **(cm^{-1}/mW)**	χ_{ps2} **(cm^{-1}/mW)**	Θ_{exp_1}	Θ_{exp_2}	Θ_{exp_3}
2.4 nm	1.59	-(0.431±0.008)	-(0.965±0.020)	-(1.253±0.031)	-(1.596±0.038)	-(3.542±0.078)	0.222±0.011	0.496±0.024	0.644±0.033
3.6 nm	1.50	-(0.325±0.013)	-(0.649±0.028)	-(0.928±0.017)	-(1.491±0.029)	-(3.245±0.051)	0.185±0.010	0.396±0.021	0.529±0.020
5.0 nm	1.43	-(0.388±0.011)	-(0.851±0.017)	-(1.138±0.020)	-(1.817±0.048)	-(3.350±0.081)	0.253±0.017	0.555±0.036	0.743±0.048
9.2 nm	1.33	-(0.375±0.008)	-(0.770±0.018)	-(1.008±0.033)	-(1.831±0.010)	-(2.937±0.077)	0.339±0.025	0.696±0.052	0.911±0.071
15.0 nm	1.30	-(0.467±0.011)	-(0.832±0.009)	-(1.014±0.014)	-(1.203±0.022)	-(2.257±0.032)	0.443±0.020	0.790±0.030	0.962±0.038
24.6 nm	1.29	-(0.273±0.005)	-(0.453±0.004)	-(0.531±0.007)	-(0.521±0.014)	-(0.899±0.016)	0.722±0.044	1.200±0.070	1.405±0.083
30.6 nm	1.29	-(0.359±0.004)	-(0.572±0.011)	-(0.662±0.005)	-(0.624±0.014)	-(1.119±0.021)	0.724±0.038	1.156±0.063	1.336±0.068
37.8 nm	1.29	-(0.421±0.011)	-(0.646±0.012)	-(0.737±0.017)	-(0.952±0.012)	-(1.557±0.027)	0.696±0.038	1.068±0.056	1.219±0.066

S4. 3D numerical modeling details

The 3D numerical modeling is based on the finite volume method. The model calculation size of the substrate has a radius and thickness of 50 μm and the MoS_2 sample is with the actual size and thickness. The smallest mesh size along the thickness direction is 0.1 nm and increases from the MoS_2 surface to the substrate with an increasing ratio of 1.02. The smallest mesh size is 1 nm in the radial direction and also increases with a ratio of 1.02. In our modeling, cross-plane thermal conductivity is $k_{\perp} = 2$ W/mK [10] for MoS_2. k_{glass}=1.4 W/mK [4]. The laser energy is set as P=1 mW for both CW laser and ps laser sources and the laser spot size varies for different heating states. As summarized in Table S1, we extract the thickness-dependent E_g values in this modeling. The reported recombination time spans from ~800 ps to 2.6 ns for SL and FL MoS_2.[11] Here, τ is set as 1 ns at room temperature as we did before.[12] And dependence of hot carrier diffusivity D on the carrier lifetime τ is discussed on S5. The carrier diffusion equation [Eq (1)] will be first solved and then the heat conduction one with the hot carrier concentration $\Delta N(\mathrm{r},t)$ used in the source term. As considered in our previous work for the interface structure, multiple reflections happen at the interface when a laser beam irradiates the sample surface.[13] Based on the Transfer Matrix Method (TMM) and the optical properties of these two materials, we could calculate the total absorption rate in MoS_2 as I_0.[14] There no laser absorption in the glass substrate. Note that for most of the heat-carrying phonons, the mean free path (MFP) of FL MoS_2 is less than 20 nm which is smaller than the laser heating size in this work. [15, 16] Therefore, in this 3D modeling, we only consider the diffusive phonon transport because the ballistic effect on thermal conductivity is not influential. The accumulative thermal conductivity as a function of the mean phonon mean free path (in-plane) will not change with lateral dimension above 1 μm (all our samples lateral size larger than 5 μm).

For the cross-plane mean free path, less work has been reported. The sample's cross-plane thermal conductivity will decrease dramatically when the thickness smaller than its cross-plane mean free path. Here, 20 nm is the total phonon MFP of MoS_2. The thermal conductivity is dominated by three acoustic phonon modes (LA, TA, ZA) owing to their large group velocities compared with optical phonon modes. For single layered MoS_2, different from single layered graphene, the contribution of the LA mode to thermal conductivity is more significant than that of the ZA mode. This is because the larger group velocity and longer relaxation time of LA phonon mode.[15] For multi-layer MoS_2, ZA mode is expected to have similar contribution (smaller than LA mode).

To show how the Five-State ET-Raman technique can eliminate the errors from the local laser absorption evaluation and temperature coefficient calibration, we do the following treatment.

Assume that we have obtained the temperature coefficient $\chi_{\mathrm{T}}(\mathrm{cm}^{-1}/\mathrm{K})$ for MoS_2. For three CW laser heating states, the temperature rise (K/mW) of MoS_2 is ΔT_1. So we express the temperature rise by the RSC as

$$\chi_{\mathrm{CW,\,MoS_2}} = \Delta T_1 \times \chi_{\mathrm{T,\,MoS_2}}. \tag{S3}$$

Because there is no laser absorption in the substrate, $\Delta T_1 \propto I_0$ which takes effect of k, R and D.

For two ps laser heating states, the temperature rise of the sample is from a single pulse heating (laser absorption from the fast thermalization process) and the steady-state accumulation of the heat. Similarly, we express the temperature rise (K/mW) of MoS_2 under 50× and 100× objectives as

$$\chi_{\mathrm{ps1,\,MoS_2}} = (\Delta T_2 + \Delta T_{\mathrm{s}}) \times \chi_{\mathrm{T,\,MoS_2}}, \tag{S4}$$

$$\chi_{\mathrm{ps2,\,MoS_2}} = (\Delta T_3 + \Delta T_\mathrm{s}) \times \chi_{\mathrm{T,\,MoS_2}}\,, \tag{S5}$$

where ΔT_2 & $\Delta T_3 \propto I_0$. ΔT_s is the temperature rise from the steady-state heat accumulation, and it is same for both the 50× and 100× states.

From the 3D simulation, for the steady-state CW laser heating, we could get ΔT_1 of MoS_2. From zero-transport state ps laser heating, we could directly get ΔT_2 and ΔT_3 by only considering the laser absorption for single pulse heating. Because the temperature rise difference of ps laser heating between 50× and 100× objective is just a function of the laser absorption of the sample, so does the normalized RSC of MoS_2.

From Eqs (S3)-(S5), we have

$$\Theta_{\mathrm{MoS_2}} = \frac{\chi_{\mathrm{CW,\,MoS_2}}}{\chi_{\mathrm{ps2,\,MoS_2}} - \chi_{\mathrm{ps1,\,MoS_2}}} = \frac{\Delta T_1}{\Delta T_3 - \Delta T_2}. \tag{S6}$$

The term ΔT_1 and $(\Delta T_3 - \Delta T_2)$ are all related to the laser absorption in MoS_2. So the normalized RSC value is now only a function of three parameters: $\Theta(k, R, D)$ and is independent of the laser absorption evaluation. For each sample, from the 3D numerical simulation and Raman experiment, we could calculate the normalized RSC (Θ_1, Θ_2, and Θ_3) for MoS_2 in the (k, R, D) space. Note the temperature rise evaluation from the simulation has considered the temperature distribution in both space and time domain as expressed by Eqs (1) and (2).

S5. The dependence of hot carrier diffusivity *D* on the carrier lifetime τ

The carrier lifetime τ takes 1 ns in our data processing by solving Eqs. (1) and (2). So the finally

determined D is dependent on the τ value. As treated in our previous work,[12] we define a normalized hot carrier concentration $\xi = \Delta N / \tau$ to re-express those equations as:

$$\Phi\alpha + D\tau\nabla^2\xi - \xi = 0\,, \tag{S7}$$

$$(h\nu - E_g)\Phi\alpha + E_g\xi + k\nabla^2\Delta T = 0\,. \tag{S8}$$

Therefore, from these two new equations without knowing other hot carrier properties, we can firmly determine the term $D\tau$ by which the lifetime diffusion length could be obtained as $L_D = \sqrt{\tau D}$. As summarized in Table S1, L_D of eight MoS_2 samples is in the order of 900 nm. Besides, the diffusivity and the mobility (μ) are related by the Einstein relation as $D / k_B T = \mu / q$ in this thermalized system, where k_B, T, and q are the Boltzmann constant, temperature, and the charge of each carrier. Here, we assume that the carriers have a thermal distribution of 300 K during the diffusion process because the energy relaxation time is only several picoseconds.[17] For the 2.4 nm thick MoS_2 sample, the measured D corresponds to mobility of μ=316.7 cm^2/Vs. Lower values of 30-60 $cm^2/V{\cdot}s$ for FL MoS_2 on SiO_2,[18] ~70 $cm^2/V{\cdot}s$ for FL MoS_2 on Al_2O_3 [19] were reported before. The possible reason is that our MoS_2 samples are unprocessed and unconstrained. Unlike the electric methods to study the carrier movement, in this work we do not cover the sample with a dielectric layer or electrical contacts. Moreover, the theoretical optical-phonon-scattering-limited mobility was reported up to 400 $cm^2/V{\cdot}s$ achieved by adopting high-κ dielectric materials (*e.g.*, HfO_2, Al_2O_3). [20-23] As discussed in our recent work, (ref) compared with c-Si substrate, the glass substrate induced dielectric environment could lead to enhanced carrier mobility especially for relatively thin MoS_2 samples.[18, 24] Also, the additional layers of thick MoS_2 would create the high dielectric environment (dielectric capping effect).[18]

Table S2. Summary of hot carrier diffusivity (D), converted electron mobility (μ), and the diffusion length (L_D) for eight FL MoS_2 samples in this work.

Sample	Number	D (cm^2/s)	μ ($cm^2/V \cdot s$)	L_D (μm)
2.4 nm	4	$7.92^{+0.82}_{-0.83}$	$316.7^{+32.9}_{-33.0}$	$0.890^{+0.287}_{-0.287}$
3.6 nm	6	$10.3^{+1.23}_{-1.06}$	$412.0^{+49.3}_{-42.5}$	$1.02^{+0.35}_{-0.33}$
5.0 nm	8	$10.2^{+1.32}_{-1.24}$	$408.0^{+52.8}_{-49.5}$	$1.01^{+0.36}_{-0.35}$
9.2 nm	15	$8.49^{+1.20}_{-1.07}$	$339.7^{+47.9}_{-42.8}$	$0.922^{+0.346}_{-0.327}$
15.0 nm	25	$10.2^{+1.15}_{-1.02}$	$408.0^{+45.9}_{-40.9}$	$1.01^{+0.34}_{-0.33}$
24.6 nm	41	$7.63^{+1.20}_{-1.09}$	$305.0^{+48.0}_{-43.6}$	$0.873^{+0.346}_{-0.330}$
30.6 nm	51	$6.45^{+1.00}_{-0.92}$	$258.1^{+37.2}_{-36.4}$	$0.803^{+0.316}_{-0.303}$
37.8 nm	63	$6.22^{+1.03}_{-0.89}$	$248.9^{+41.2}_{-35.6}$	$0.789^{+0.321}_{-0.298}$

References

1. S. Berciaud, M. Y. Han, K. F. Mak, L. E. Brus, P. Kim and T. F. Heinz, *Physical review letters*, 2010, **104**, 227401.
2. A. K. Vallabhaneni, D. Singh, H. Bao, J. Murthy and X. Ruan, *Physical Review B*, 2016, **93**, 125432.
3. S. Sullivan, A. Vallabhaneni, I. Kholmanov, X. Ruan, J. Murthy and L. Shi, *Nano letters*, 2017, **17**, 2049-2056.
4. T. L. Bergman and F. P. Incropera, *Fundamentals of Heat and Mass Transfer*, John Wiley & Sons, 2011.
5. P. Yuan, T. Hong, W. Ridong, W. Tianyu and W. Xinwei, *RSC Advances*, 2018, **8**, 12767-12778.
6. P. Yuan, C. Li, S. Xu, J. Liu and X. Wang, *Acta Mater.*, 2017, **122**, 152-165.
7. W. Cai, A. L. Moore, Y. Zhu, X. Li, S. Chen, L. Shi and R. S. Ruoff, *Nano Lett.*, 2010, **10**, 1645-1651.
8. C. Yim, M. O'Brien, N. McEvoy, S. Winters, I. Mirza, J. G. Lunney and G. S. Duesberg, *Appl. Phys. Lett.*, 2014, **104**, 103114.
9. Q. H. Wang, K. Kalantar-Zadeh, A. Kis, J. N. Coleman and M. S. Strano, *Nat. Nanotechnol.*, 2012, **7**, 699-712.
10. J. Liu, G.-M. Choi and D. G. Cahill, *J. Appl. Phys.*, 2014, **116**, 233107.
11. H. Shi, R. Yan, S. Bertolazzi, J. Brivio, B. Gao, A. Kis, D. Jena, H. G. Xing and L. Huang, *ACS Nano*, 2013, **7**, 1072-1080.
12. P. Yuan, J. Liu, R. Wang and X. Wang, *Nanoscale*, 2017, **9**, 6808-6820.
13. P. Yuan, R. Wang, H. Tan, T. Wang and X. Wang, *ACS Photonics*, 2017, **4**, 3115-3129.
14. E. X. Pérez, *Design, fabrication and characterization of porous silicon multilayer optical devices*, Universitat Rovira i Virgili, 2008.
15. J. J. Bae, H. Y. Jeong, G. H. Han, J. Kim, H. Kim, M. S. Kim, B. H. Moon, S. C. Lim and Y. H. Lee, *Nanoscale*, 2017, **9**, 2541-2547.
16. Y. Cai, J. Lan, G. Zhang and Y.-W. Zhang, *Phys. Rev. B*, 2014, **89**, 035438.
17. Z. Nie, R. Long, L. Sun, C.-C. Huang, J. Zhang, Q. Xiong, D. W. Hewak, Z. Shen, O. V. Prezhdo and Z.-H. Loh, *ACS nano*, 2014, **8**, 10931-10940.
18. W. Bao, X. Cai, D. Kim, K. Sridhara and M. S. Fuhrer, *Appl. Phys. Lett.*, 2013, **102**, 042104.
19. W. Choi, M. Y. Cho, A. Konar, J. H. Lee, G. B. Cha, S. C. Hong, S. Kim, J. Kim, D. Jena and J. Joo, *Adv. Mater.*, 2012, **24**, 5832-5836.
20. B. Radisavljevic, A. Radenovic, J. Brivio, i. V. Giacometti and A. Kis, *Nat. Nanotechnol.*, 2011, **6**, 147-150.
21. H. Liu and D. Y. Peide, *IEEE Electron Device Lett.*, 2012, **33**.
22. H. Wang, L. Yu, Y.-H. Lee, W. Fang, A. Hsu, P. Herring, M. Chin, M. Dubey, L.-J. Li and J. Kong, 2012.
23. K. Kaasbjerg, K. S. Thygesen and K. W. Jacobsen, *Phys. Rev. B*, 2012, **85**, 115317.
24. S.-L. Li, K. Wakabayashi, Y. Xu, S. Nakaharai, K. Komatsu, W.-W. Li, Y.-F. Lin, A. Aparecido-Ferreira and K. Tsukagoshi, *Nano Lett.*, 2013, **13**, 3546-3552.